


Some observations on Reynolds number scaling in wall-bounded flows

Alexander J. Smits **Mechanical and Aerospace Engineering, Princeton University, Princeton, New Jersey 08544, USA*(Received 5 August 2020; accepted 15 September 2020;
published 24 November 2020)

High Reynolds number wind tunnels are essential tools for testing theories of turbulence. This need has led to the construction of tunnels that use compressed gases as the working fluid, and such facilities have given new insights into the behavior of turbulence in wall-bounded flows. Here, we focus on results obtained at Princeton using the Superpipe and the High Reynolds number Testing Facility that have given us new insights into the behavior of wall-bounded flows, in particular, fully developed pipe flow, and turbulent boundary layers in zero pressure gradients.

DOI: [10.1103/PhysRevFluids.5.110514](https://doi.org/10.1103/PhysRevFluids.5.110514)

I. INTRODUCTION

In this paper, I discuss the results obtained in the Superpipe and the High Reynolds number Testing Facility (HRTF) at Princeton on Reynolds number scaling in wall-bounded turbulence. The content follows the Otto Laporte Lecture, delivered at the APS/DFD meeting in Seattle, WA, on 24 November 2019.

The Princeton facilities use compressed air as the working fluid, with operating pressures up to 200 bar to achieve a wide range of Reynolds numbers, and they have helped to give new insights into the behavior of fully developed pipe flow and flat plate turbulent boundary layers. In particular, the experiments confirmed the logarithmic scaling of both the mean flow and the streamwise turbulence intensity at sufficiently high Reynolds number, and provide robust support for the attached eddy model of turbulence.

Naturally, the need for experiments at high Reynolds number has been recognized since the inception of research on turbulence. Many of our most fundamental theories of turbulence, for example the appearance of a $-5/3$ region in the spectrum, were derived in the limit of infinite Reynolds number. Such theories required testing, and some researchers turned to geophysical flows to have access to very high Reynolds numbers. For example, the experiments by Grant *et al.* [1] investigated turbulence in a tidal channel, achieving Reynolds numbers of about 3×10^8 (based on the depth of the channel and the mean velocity). R. J. Taylor [2] was motivated by a similar aim in his study of turbulence in the atmospheric boundary layer, and indeed some of the earliest work on turbulence in the atmosphere was done by G. I. Taylor [3].

It was also understood that the proper design of airplanes, for example, required a full understanding of Reynolds number scaling. The drag on the vehicle, its stall characteristics, and the formation of wakes, were all known to depend on Reynolds number, and so the necessity to perform tests at flight Reynolds numbers was a powerful driver for the design and construction of new kinds of wind tunnels. Large tunnels, however, are expensive to build and run, and high flow velocities may introduce compressibility effects.

In a landmark contribution, Munk [4] suggested instead using air at variable pressure to achieve a wide range of Reynolds numbers on a modest scale. Because the dynamic viscosity of air increases

*asmits@princeton.edu

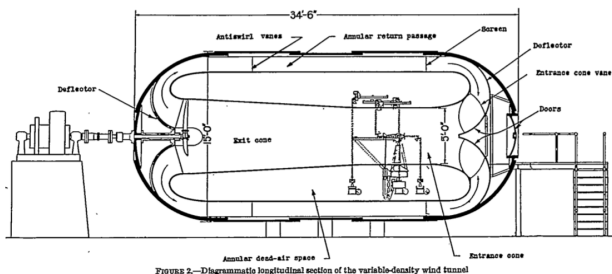
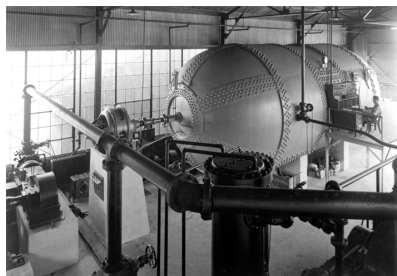


FIG. 1. Langley Variable Density Tunnel, completed 1923 [5,6]. Operating conditions: $p = 0.1$ to 20 bar (abs), $D = 1.5$ m, $L = 1.8$ m, $V_m = 20$ m/s, $Re_m = 26 \times 10^6/m$.

only slowly with pressure, the Reynolds number increases almost in proportion to the increase in pressure. Munk's vision was realized in 1923 with the construction of the Langley Variable Density Tunnel, shown in Fig. 1 [5,6]. A more-or-less conventional wind tunnel was contained within a large pressure vessel capable of operating at pressures from 0.1 to 20 bar (abs), achieving Reynolds numbers up to $Re_m = 5.3 \times 10^6/m$ at a maximum tunnel speed V_m of only 20 m/s (see also Table I). The facility was used mainly for aeronautical studies, and yielded, among other advances, the emblematic NACA nacelle design. In 1941 it was superseded by the Langley two-dimensional low-turbulence pressure tunnel (LTPT) which also featured variable pressure while having much improved flow conditions [7]. The LTPT ran at pressures up to 10 bars and at Reynolds numbers of up to about $Re_m = 40 \times 10^6/m$. It was operational till 2006.

The concept of variable pressure was also used in the construction of the Compressed Air Tunnel at the National Physical Laboratory in Teddington in 1931 [8,19]. In its 6 ft diameter test section, air could be compressed up to 25 bars to produce Reynolds numbers up to $Re_m = 45 \times 10^6/m$. As with the VDT, the main focus of the Compressed Air Tunnel was improving the aerodynamic performance of aircraft. Similarly, the RAE 5m tunnel and the ONERA F1 tunnel [11,12] were designed as production tunnels for aeronautical purposes (see Table I). Bodenschatz *et al.* [17] is a good source for additional background on the development of variable pressure tunnels.

Relatively few experiments were conducted in such facilities to address fundamental questions in turbulence. Kistler and Vrebalovich [20] were able to conduct a classical grid turbulence experiment at the Southern California Cooperative Wind Tunnel at wind speeds of up to 60 m/s and with

TABLE I. Characteristics for selected high pressure wind tunnels.

Tunnel	Year	Ref.	P (bar)	D (m)	L (m)	V_m (m/s)	Re_m/m
Langley VDT	1923	[5]	0.1–4	1.5	1.8	20	5.3×10^6
NPL CAT	1931	[8]	1–25	1.8	≈ 5	27	45×10^6
Langley LTPT	1941	[7]	1–10	0.9×2.3	2.3	150	40×10^6
SCCWT	1945	[9]	0.1–3	3.7×2.6	5.5	170	230×10^6
NRL Jülich	??	[10]	1–40	0.75	4	15	40×10^6
RAE 5m	1973	[11]	1–3	5×4	12	110, 94	20×10^6
ONERA F1	1977	[12]	1–4	4.5×3.5	11	120, 80	32×10^6
Göttingen HDG	1981	[13]	1–100	0.6	1	35	120×10^6
PU Superpipe	1994	[14]	1–200	0.129	22	35	350×10^6
Stanford	1999	[15]	1–8	0.15	3	17	8.5×10^6
PU HRTF	2007	[16]	1–200	0.5	3.6	10	90×10^6
MPIDS VDTT	2014	[17]	0.1–15	1.5×1.3	8.8	4.1	34×10^6
PU Supertank	2021	[18]	1–80	0.88	7.5	14	60×10^6

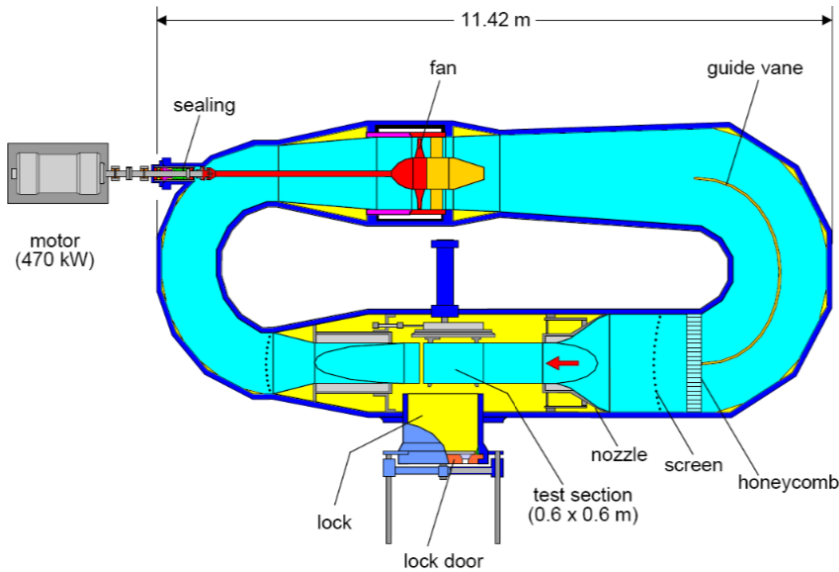


FIG. 2. Göttingen high pressure tunnel, completed 1981. Operating conditions: $p = 1$ to 100 bar (abs), $D = 0.6$ m diam., $L = 1$ m, $V_m = 35$ m/s, $Re_m \approx 200 \times 10^6/m$. Reproduction with permission from [24].

air pressures between 0.2 bar and 4 bars to achieve Reynolds numbers up to $Re_m = 16 \times 10^6/m$ (grid Reynolds numbers up to 2.4×10^6). Another series of fundamental studies in pressurized tunnels was conducted on the flow past spheres at the Nuclear Research Laboratories in Jülich in the 1970s [10]. The wind tunnel there could be pressurized up to 40 bars. Another notable variable pressure facility is the high pressure wind tunnel (HDG) at the German Aerospace Center (DLR) in Göttingen [13], which can be operated at pressures up to 100 bars and speeds up to 35 m/s, so that Reynolds numbers up to $200 \times 10^6/m$ are possible (see Fig. 2). It has been used to study flow-induced vibration [21], and to investigate the flow over a circular cylinder for $10^4 < Re_D < 10^7$ [22,23].

I mention these facilities to emphasize that the concept of using high pressure to obtain high Reynolds numbers is now almost 100 years old, and that this approach has been put into practice a number of times. However, the concept of Superpipe, which was always envisioned purely as a research tool for studying Reynolds number effects on turbulence, only originated in 1990 as part of discussions at the AFOSR workshop on “New Approaches to Experimental Turbulence Research,” held at Princeton University in 1990 [25]. There, Fazle Hussain remarked: “I think some national or large-scale centers are unavoidable, so that large, unique facilities can be shared by all qualified researchers. One example of specific experiments that I have proposed a few years back is a pipe, of the order of 5 m in diameter, 5 km long.” Bill George added: “I agree that we need high Reynolds number facilities. Answers from these facilities may prove to generate lots of ideas and a lot of things we take for granted may prove to be wrong and we won’t know until we push toward higher Reynolds number.” Tony Perry pointed out that the cost of such a facility is really not so great when one considers that a billion dollar facility which produces a Reynolds number of a billion “works out to only one dollar per unit Reynolds number!” A particularly perspicacious comment came from Bert Hesselink, who observed that “the power requirements for a high Reynolds number facility scale as L^3 . So there is much to be said for making the facility smaller and putting our efforts in areas where other technologies have been developed, such as in micro-electronics and micro-optics. This underrates the idea of developing more instrumentation. We should go smaller and put resources in areas where problem really exists—in the measurements.”



FIG. 3. Left: Princeton High Reynolds number Testing Facility (HRTF), completed 2007. Operating conditions: $p = 1$ to 200 bar (abs), $D = 0.5$ m dia., $L = 3.6$ m, $V_m = 10$ m/s, $Re_m \approx 90 \times 10^6$ /m. Right: Princeton Superpipe, completed 1994. Operating conditions: $p = 1$ to 200 bar (abs), $D = 0.129$ m dia., $L = 22$ m, $V_m = 35$ m/s, $Re_m \approx 270 \times 10^6$ /m. Reproduction with permission from D. Quinn.

The idea of using high pressure to keep the facility a reasonable size came up at a dinner during the workshop attended by Steve Orszag, Katepalli Sreenivasan, Victor Yakhot, Garry Brown, and Fazle Hussain. The next morning, Steve mentioned to me the suggestions from dinner. I did some quick estimates for a high Reynolds number experiment using a 6 in. pipe and found all the numbers on scale and power requirements to be feasible for a laboratory environment.

Steve's research on turbulence was supported in part by ARPA's Mathematics Directorate, and in his next proposal to ARPA he wanted to include an experiment on pipe flow turbulence at high Reynolds number. The proposal was successful, and I was lucky enough to recruit Mark Zagarola to design and build the pipe, later to be called "Superpipe" by Steve. It could achieve a bulk flow Reynolds number of about 35×10^6 and it cost about \$300 000, which Steve noted was less than one cent per Reynolds number, two orders of magnitude less than the tongue-in-cheek estimate put forward by Tony Perry. The design was first reported in 1992 [26], and it was operational by 1994. It is shown in Fig. 3; the full details of its design and construction are given by Zagarola [14]. Briefly, it operates from atmospheric pressure up to 200 bar with speeds up to 35 m/s to obtain a variation in Reynolds number of three orders of magnitude, that is, $31 \times 10^3 \leq Re_D \leq 35 \times 10^6$ ($10^3 \leq Re^+ \leq 5 \times 10^5$). Here, $Re_D = 2R\bar{U}/\nu$ and $Re^+ = Ru_\tau/\nu$, where R is pipe radius, \bar{U} is the bulk velocity, $u_\tau = \sqrt{\tau_w/\rho}$, ρ is the fluid density, μ is the viscosity, and $\nu = \mu/\rho$ is the kinematic viscosity. More generally, $Re^+ = \delta u_\tau/\nu$, where δ is the characteristic width of the flow (the boundary layer thickness, the pipe radius, or the channel half-height). Although Superpipe has a length of only 22 m and an internal diameter of 0.129 m, if the same facility was operated using atmospheric air at 30 m/s, then at the highest Reynolds number it would be equivalent to a pipe that is 3200 m long and 1.6 m diameter, which is getting close to the facility suggested by Fazle Hussain.

Since the Superpipe was completed, a number of other compressed-gas facilities have been constructed for the similar purpose of examining fundamental questions in turbulence. The Stanford high pressure tunnel was completed in 1999 by Eaton and DeGraaff [15,27] in order to study turbulent boundary layers, and it operates at pressure up to 8 atm (see Table I). There is also the Variable Density Turbulence Tunnel in Göttingen, Germany [17], which can operate with a variety of gases. To reach the highest Reynolds numbers the tunnel is pressurized to 15 bar with the dense gas SF₆.

A little earlier, in 2007, the High Reynolds number Testing Facility (HRTF), shown in Fig. 3, was completed at Princeton [16]. This wind tunnel operates at pressures up to 200 atm, and it can generate turbulent boundary layers at Reynolds numbers over the range $8400 \leq Re_\theta \leq 235\,000$, that is, $2600 \leq Re^+ \leq 72\,500$. Here, $Re_\theta = \theta U_\infty/\nu$, θ is the momentum thickness and U_∞ is the freestream velocity. With atmospheric air at 10 m/s, it yields a Reynolds number that is equivalent

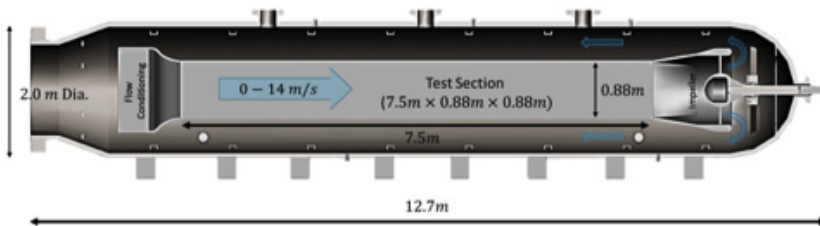


FIG. 4. Princeton Supertank, expected completion 2021. Reproduction with permission from [18]. Operating conditions: $p = 1$ to 80 bar (abs), $H = 0.88$ m diam., $L = 7.5$ m, $V_m = 14$ m/s, $Re_D \approx 60 \times 10^6/m$.

to a tunnel with a working section 800 m long and 80 m diameter. There is also a new facility under construction at Princeton, the Supertank [18]. It is expected to be in service in 2021, operating at pressure up to 80 atm (see Fig. 4 and Table I). With atmospheric air at 14 m/s, at the highest Reynolds number it would be equivalent to a tank 1000 m long with a diameter of 160 m [28].

Here, we focus on the results obtained in the Superpipe facility and the HRTF, complemented by data on turbulence structure acquired in a pipe flow facility at Princeton using water as the working fluid. Where possible, the data will be interpreted in terms of the attached eddy models due to Townsend [29] and Perry and Chong [30]. There are a number of other theoretical development that relate to turbulence scaling, and some notable references are McKeon and Sharma [31], Monkewitz and Nagib [32], and Taira *et al.* [33], and the references included therein. In this paper, however, the interpretations will be made primarily in the context of the attached eddy model. The paper will conclude with some recommendations for future research.

II. TURBULENT WALL-BOUNDED FLOWS AND REYNOLDS NUMBER

A number of different Reynolds numbers are in use, but to describe the scaling of wall-bounded flows we generally use the friction Reynolds number, Re_τ or Re^+ , defined earlier as $Re^+ = \delta u_\tau / \nu$, where $u_\tau = \sqrt{\tau_w} / \rho$ is the friction velocity. The friction Reynolds number can be interpreted as the ratio of two scales of motion, where δ is characteristic of the size of the largest eddies in the flow, and ν / u_τ is characteristic of the size of the smallest eddies (the Kolmogorov length scale η in wall-bounded flows near the wall is typically about two to four times larger than ν / u_τ [34]). Hence, the friction Reynolds number expresses somewhat quantitatively the scale separation that is characteristic of turbulence, and how this scale separation increases with Reynolds number. In Fig. 5, this feature is qualitatively illustrated using flow visualizations of boundary layers at two different Reynolds numbers.

As indicated in the Introduction, a first-order question in turbulence research is to understand the behavior of turbulence at asymptotically high Reynolds numbers, that is, at Reynolds numbers where the smallest scales are expected to be independent of the large scales. This question is more

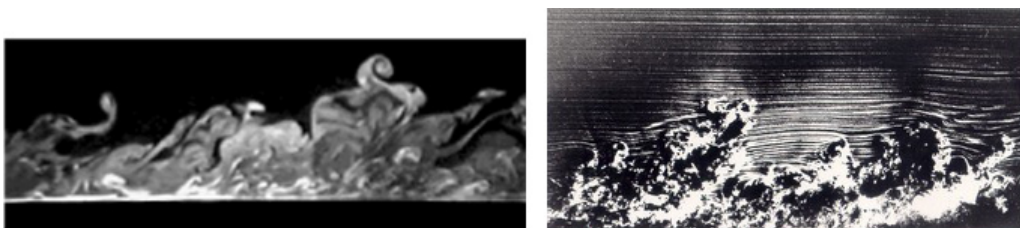


FIG. 5. Turbulent boundary layer visualizations, flow from left to right. Left: $Re_\tau \approx 150$. Reproduction with permission from [35]. Right: $Re_\tau \approx 1100$ ($Re_\theta \approx 2600$). Reproduction with permission from [36].

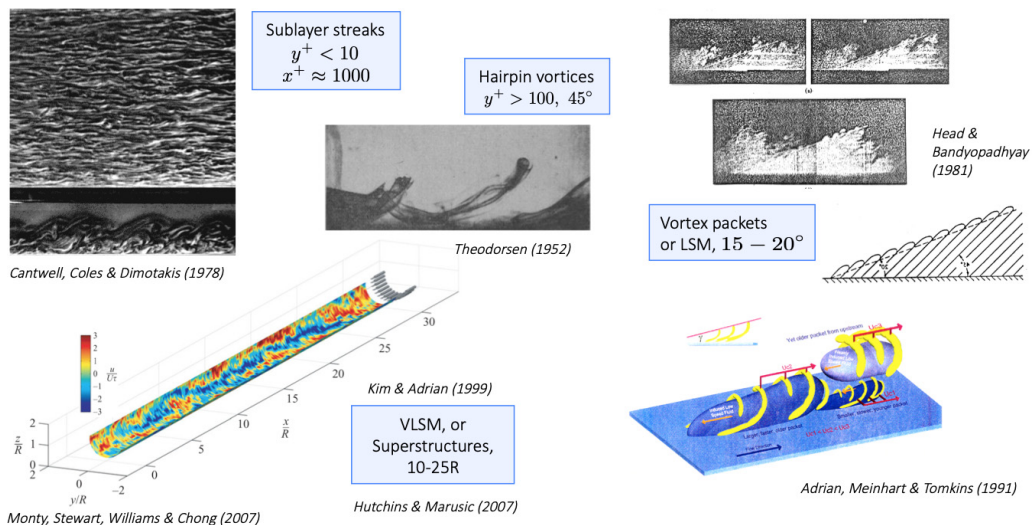


FIG. 6. Coherent motions in wall-bounded turbulence. Illustrations of sublayer streaks [41]; hairpin vortices [42]; vortex packets or large scale motions (LSM) [30,43,44]; very large scale motions (VLSM) or superstructures [38,40,45]. All figures reproduced with permission from respective sources.

often examined in studies of homogeneous turbulence, but it is also relevant to wall-bounded flows where the geometric (impermeability), kinematic (no-slip), and dynamic (shear force) constraints presented by the wall exert a decisive influence on the eddy shape and size. In particular, wall-bounded turbulence features a number of different types of organized motions that are loosely organized into “families” that reveal their full form only at a high enough Reynolds number where there is a sufficient scale separation [37].

There are essentially four different but interrelated families. The structures located nearest the wall are the sublayer streaks (see Fig. 6), which are associated with elongated vortex motions having characteristic dimensions of $x_s^+ \approx 1000$, $y_s^+ < 10$, and $z_s^+ \approx 100$. Here x is the streamwise direction, y is the wall-normal direction, and z is the spanwise direction, and the “plus” notation indicates that the scales are normalized by the viscous length scale ν/u_τ . The next family contains the hairpin or Λ vortices, with $z_s^+ = O(100)$, a height that scales with the distance from the wall, and these vortices lean downstream at a typical angle of about 45° . The hairpin vortices are often found to be organized within a larger scale structure called vortex packets, or, more anonymously, large scale motions (LSM), which makes up the third family of organized motions. Within the LSM, the heads of the hairpin vortices tend to align along a direction that is inclined to the wall by about 15° or 20° . LSM have a streamwise scale of approximately $2\delta-3\delta$ and are associated with the occurrence of bulges of turbulent fluid at the edge of a boundary layer. The fourth family is made up of even larger structures which are up to $10\delta-20\delta$ long, called very large scale motions (VLSM) in pipe flow and superstructures in boundary layers. Recent evidence indicates that VLSM are composed of a meandering train of LSM (see, for example, [38,39]), as first suggested by [40]. The energy content of the VLSM increases with Reynolds number, and so the energy content of wall-bounded flows changes slowly with Reynolds number from one that is dominated by hairpin vortices and LSM to one that is dominated by LSM and VLSM.

III. MEAN FLOW SIMILARITY

The Navier-Stokes equation indicates that in the near-wall region where viscosity dominates the mean velocity profile is linear, so that $U^+ = y^+$, where $U^+ = U/u_\tau$, $y^+ = yu_\tau/\nu$, and U is the mean velocity in the streamwise or x -direction. That is, the length and velocity scales for the inner region

are the viscous length scale ν/u_τ and the friction velocity u_τ . Farther from the wall the influence of viscosity diminishes, and at distances sufficiently far from the wall the length scale will be set by the thickness of the layer, that is, the outer length scale δ . It is normally assumed that the outer velocity scale is the same as the inner velocity scale u_τ . In this respect, Townsend [29] argued that the inner region presents something like a translation velocity to the outer layer, and since this translation velocity is set by the wall shear, u_τ is the correct velocity scale for the outer as well as the inner regions. Accordingly, dimensional analysis gives that the dependence of the velocity at any point in the layer is given by

$$U = \phi(y, \tau_w, \mu, \rho, \delta).$$

Near the wall in terms of outer variables, that is, for $y/\delta \ll 1$, we expect there to be a region where the outer length scale is not important, so that we have inner scaling where

$$U^+ = f(y^+),$$

which reduces to $U^+ = y^+$ in the viscous sublayer. Far from the wall in terms of inner variables, that is, for $y^+ \gg 1$, we expect there to be a region where the viscosity is not important, so that we have outer scaling where

$$U_\infty^+ - U^+ = g(y/\delta),$$

where U_∞ is the freestream velocity for a boundary layer and the centerline velocity for a pipe or channel. Note that this relationship is written in defect form, that is, in terms of the difference between the freestream or centerline velocity and the local velocity. This approach resonates with Townsend's notion of a translation velocity.

Millikan [46] proposed that in the region sufficiently far from the wall but still far from the edge of the layer, there may be a region where neither length scale is relevant, and by matching the velocity gradients in this "overlap" region (also called the "constant stress," "equilibrium," "inertial," or "logarithmic" region) we obtain

$$U^+ = \frac{1}{\kappa} \ln y^+ + B, \quad (1)$$

or, equivalently,

$$U_\infty^+ - U^+ = -\frac{1}{\kappa} \ln \frac{y}{\delta} + B_1. \quad (2)$$

Here, κ is the von Kármán constant, and B and B_1 are known as the additive constants. Because the degree of scale separation is expressed by the friction Reynolds number Re^+ , we expect that this overlap region will increase in size with increasing Reynolds number.

This logarithmic variation in the intermediate zone was always considered to be one of the cornerstones of our understanding of wall-bounded flows. However, the Superpipe mean flow data showed some deviations which were initially widely disputed. As shown in inner coordinates [as used in (Eq. (1)) in Fig. 7, for the region $50 \lesssim y^+ \lesssim 300$ the velocity variation is not logarithmic but follows more closely a power law (see [47] for details). The log law will then appear in the interval $600 < y^+ < 0.12\text{Re}^+$, which means is that the log law only appears in pipes for Re^+ greater than approximately 5000. A similar behavior has since been seen for boundary layers although the upper limit on y^+ is somewhat smaller [48]. Also, for the higher Reynolds number flows where a log law is evident, its slope did not correspond to the generally accepted value for κ of 0.41, but it was somewhat larger, more in accordance with an earlier study by Patel [49]. See also [47]. Later work by Bailey *et al.* [50] demonstrated the difficulties of measuring κ accurately, even in pipe flow where it is possible to measure u_τ to better than 1% accuracy. Bailey *et al.* recommended that the best estimate for κ as measured in the Superpipe was most likely 0.40 ± 0.02 , in accordance with the generally accepted value.

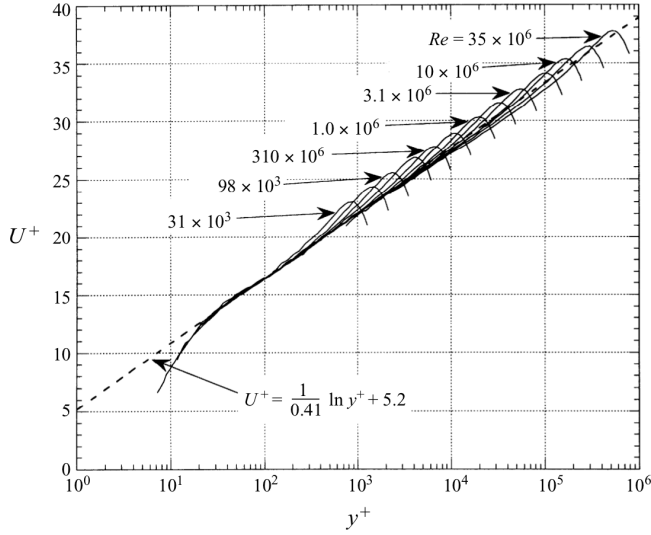


FIG. 7. Superpipe mean velocity results for $850 \leq Re_\tau \leq 500\,000$ in inner scaling. Reproduction with permission from [51].

The same mean flow results are displayed in Fig. 8 in two different forms. On the left the data are shown in classical outer layer coordinates [as used in Eq. (2)], and what is evident is a persistent trend with Reynolds number for $Re_D < 10^6$ ($Re^+ < 20\,000$). On the right, they are shown in what is now sometimes called Zagarola scaling. That is, instead of the friction velocity we use an outer velocity scale u_o defined by $u_o = U_{CL} - \bar{U}$, where \bar{U} is the bulk velocity. For a boundary layer, the equivalent scale is $u_o = \delta^*/\delta$, where δ^* is the displacement thickness [52]. It is in some sense a “true” outer velocity scale since it is independent of the wall shear. As Zagarola and Smits [53] concluded, for Reynolds numbers Re_D between 31×10^3 and 540×10^6 ($850 < Re^+ < 11\,000$), it appears that u_o is a better outer velocity scale than u_τ [14]. This result further reinforces the notion that viscous effects reach farther from the wall than previously understood, and in pipe flows the outer region only reaches its asymptotic state at very high Reynolds numbers.

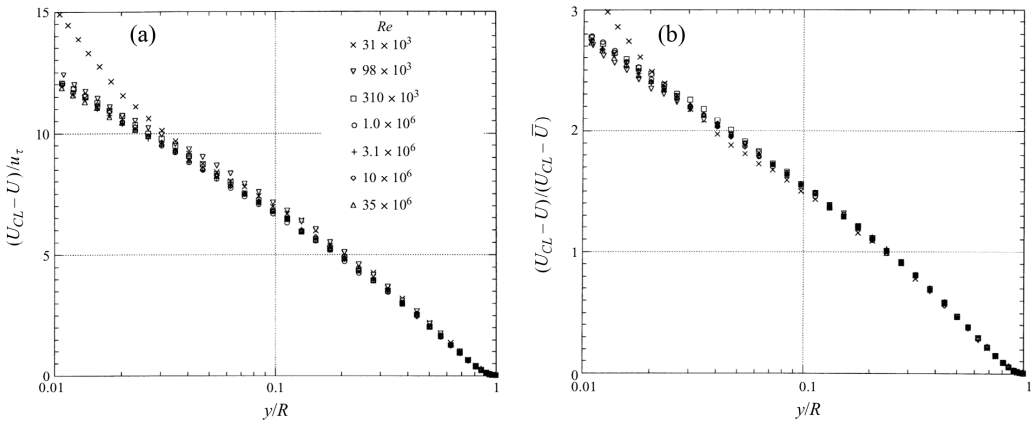


FIG. 8. Superpipe mean velocity results for $850 \leq Re_\tau \leq 500\,000$. (a) Classic outer scaling. (b) Zagarola outer scaling. Reproduction with permission from [51].



FIG. 9. Left: Townsend roller eddies. Reproduction with permission from [29]. Middle: Theodorsen hairpin eddies. Reproduction with permission from [42]. Right: Perry and Chong's wall-attached eddies. Reproduction with permission from [30].

Parenthetically, u_o has been found to be a useful scale to collapse turbulent boundary layer data in adverse and favorable pressure gradients [54], as well as flows with suction or blowing [53].

IV. ATTACHED EDDY HYPOTHESIS

One of the most successful concepts for scaling the turbulence is the idea of attached eddies, first put forward by Townsend [29]. Townsend proposed that in the equilibrium region (the region large compared to the viscous layer and small compared to the overall size of the flow), the turbulent transport of momentum was dominated by eddies of a size that scaled with distance from the wall. "In other words, the velocity fields of the main eddies, regarded as persistent, organized flow patterns, extend to the wall and, in a sense, they are attached to the wall." His attached eddy model (AEM) is an inviscid (high Reynolds number) model, and proposes a superposition of geometrically self-similar, attached eddies. The eddies cover a wide range of scales, but each scale is proportional to the distance from the wall, and all the eddies have the same characteristic velocity scale, u_τ . Townsend proposed that they might resemble roller eddies, as shown in Fig. 9. The model was designed to give $-\overline{uv}/u_\tau^2 = 1$ and it applies only in the constant stress (equilibrium) region. Townsend's model then predicts that, at sufficiently high Reynolds number,

$$\frac{\overline{u^2}}{u_\tau^2} = B_1 - A_1 \ln\left(\frac{y}{\delta}\right), \quad (3)$$

$$\frac{\overline{v^2}}{u_\tau^2} = A_2, \quad (4)$$

$$\frac{\overline{w^2}}{u_\tau^2} = B_3 - A_3 \ln\left(\frac{y}{\delta}\right). \quad (5)$$

The AEM was developed much more extensively by Perry and Chong [30] and given a physical basis by incorporating specific eddy shapes. As they noted, "In this theory, wall turbulence is considered to consist of a 'forest' of randomly positioned horseshoe, hairpin or Λ -shaped vortices that lean in the streamwise direction and have their legs extending to the wall." The eddy shapes and size distributions were drawn directly from experimental observations, notably the Theodorsen hairpin eddies [42,55] and the vortex packets described by Head and Bandyopadhyay [43].

The model by Perry and Chong is well illustrated by Fig. 10. The eddies are assumed to be made up of two rodlike vortices, joined at their apex and leaning downstream at 45° , with a width equal to their height, and a velocity scale given by u_τ . In this discrete representation, the smallest eddies (the first hierarchy) have a width/height of $100v/u_\tau$, chosen to match the characteristic spanwise scaling of the sublayer streaks. Even the smallest eddies are taken to be large enough so that viscous effects are negligible. The next hierarchy is twice the size, and contains half the number of eddies, and so on. The largest eddies are of a size corresponding to the furthest extent of the equilibrium region. Each hierarchy scales geometrically with the distance from the wall, so that the number of eddies per unit area scales with $1/y^2$. All the eddies have the same velocity scale u_τ . The induced velocity field due to all the vortex rods can then be summed to give the mean velocity and turbulence

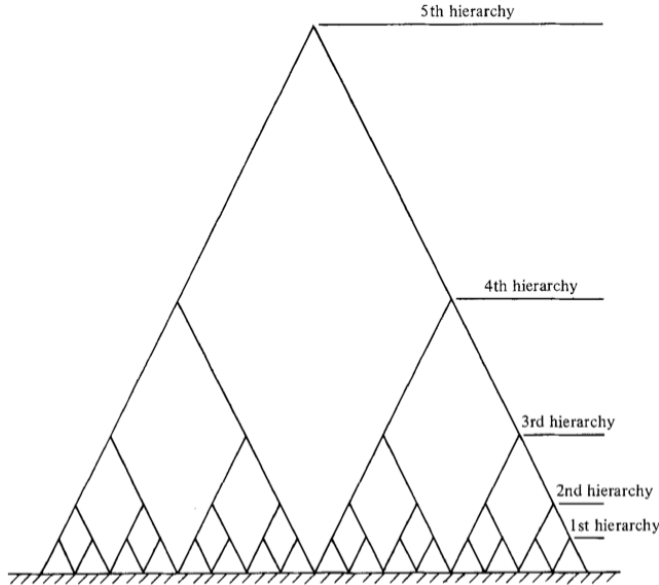


FIG. 10. Perry and Chong's hierarchy of attached wall eddies. Reproduction with permission from [30].

distributions. The actual model assumes that within each hierarchy there is a distribution of eddy sizes (hence the word hierarchy) so that the mean velocity and turbulence distributions are smooth with wall distance (see Fig. 9).

It is somewhat straightforward to see that the model inherently gives a logarithmic distribution in the mean velocity. The circulation at any distance from the wall is proportional to the number of vortex rods present at that height. For a two-dimensional wall-bounded flow the mean vorticity is given by $-dU/dy$ (the contribution from dV/dx generally being negligible), and so it is evident that for this hierarchical structure $dU/dy \sim y^{-1}$, which yields a logarithmic variation of the mean velocity. Hence, the model intrinsically yields the mean flow logarithmic scaling, which Townsend's model did not. It also reproduces the scaling given by Eqs. (3)–(5), and the form of the spectrum, including the -1 and $-5/3$ regions. These forms are obtained by summing the various components of the velocity field induced by the vortex arrays [30].

The Perry and Chong AEM therefore gives specific and powerful predictions regarding the scaling of the mean flow and the turbulence, and demonstrates that the potential-flow Λ vortex provides a link between the mean flow, Reynolds shear stress, turbulence intensities, and spectra in wall turbulence. For a more up-to-date and much more explicit description of the AEM, see Marusic and Monty [56].

The scaling given by Eqs. (3)–(5) can also be derived from spectral considerations. As Perry and Abell [57] showed for the region in space that is populated by wall-attached eddies, with sufficient scale separation (high enough Reynolds number) three regions in the one-dimensional, streamwise turbulence spectrum may be identified: a low-wave-number region corresponding to large-scale nonuniversal motions that obey outer flow scaling, a mid-wave-number region of universal wall-structure where the eddies scale with y^{-1} (that is, wall-attached scaling), and a high-wave-number inertial region that scales with the Kolmogorov length scale η . For pipe flow, the three regions are then described by

$$\frac{\phi_{11}(k_1 R)}{u_\tau^2} = g_1(k_1 R), \quad (6)$$

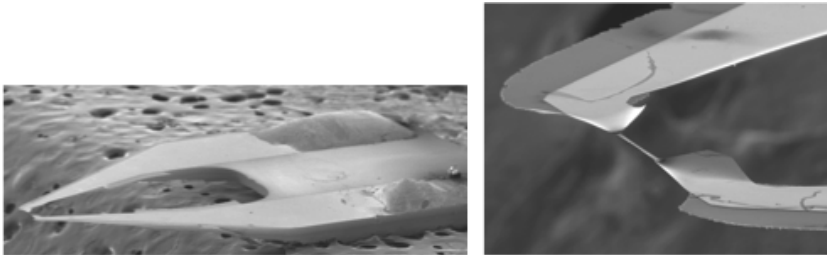


FIG. 11. NSTAP probe design [60–62].

$$\frac{\phi_{11}(k_1 y)}{u_\tau^2} = g_2(k_1 y), \quad (7)$$

$$\frac{\phi_{11}(k_1 \eta)}{u_\tau^2} = g_3(k_1 \eta). \quad (8)$$

At a high enough Reynolds number, it was proposed that there may exist two overlap regions in wave-number space: one between the R - y regions and one between the y - η regions. In these overlap regions, we then expect

$$\frac{\phi_{11}(k_1 R)}{u_\tau^2} = \frac{A_1}{k_1 R}, \quad (9)$$

$$\frac{\phi_{11}(k_1 \eta)}{u_\tau^2} = \frac{K_0}{(k_1 \eta)^{-5/3}}. \quad (10)$$

So this overlap argument yields a k^{-1} region and a $k^{-5/3}$ region in the wave-number spectrum, the latter obviously corresponding to the well-known Kolmogorov region. In the premultiplied representation, the spectrum is expected to show a constant plateau in the k_1^{-1} region, with an amplitude of A_1 . By integration of the spectrum, Perry and Abell [57] then recovered the logarithmic scaling for the streamwise component given by Eq. (3), with the addition of an additive viscous correction term that becomes negligible at asymptotically high Reynolds numbers. Therefore the constant A_1 in Eq. (9) is the same as that given in Eq. (3). These arguments were expanded to include the other components of the turbulence as well as the shear stress by Perry *et al.* [58].

V. TURBULENCE SIMILARITY

One of the difficulties in the experimental verification of the turbulence scaling is that viscous effects remain important even at moderate Reynolds numbers [59]. The advantage of using high pressure air as the working fluid is that it becomes possible to examine these scaling laws at very high Reynolds number. However, the principal disadvantage is that spatial resolution of the instrumentation can become a major issue. For example, at $\text{Re}_D = 6 \times 10^6$ ($\text{Re}^+ = 98 \times 10^3$), the viscous length scale in the Superpipe (diameter 0.129 m) is $1.3 \mu\text{m}$, and so a regular hot wire of length $\ell = 1 \text{ mm}$ would have $\ell^+ = \ell u_\tau / \nu \approx 760$ at this Reynolds number, which would lead to an unacceptable level of spatial filtering. This problem sparked a long development program at Princeton to manufacture much smaller probes [60–62]. As a result, the NanoScale Thermal Anemometry Probe (NSTAP) was introduced in 2010, with subsequent refinements leading to probes as small as $\ell = 30 \mu\text{m}$. An early $60 \mu\text{m}$ example is shown in Fig. 11. Another advantage offered by these small probes is an excellent frequency response, extending to 200–250 kHz.

Nevertheless, for measurements in the Superpipe even a $30 \mu\text{m}$ probe gives $\ell^+ = 23$ at $\text{Re}_D = 6 \times 10^6$ ($\text{Re}^+ = 98 \times 10^3$). It became clear that accurate estimates of the turbulence behavior close

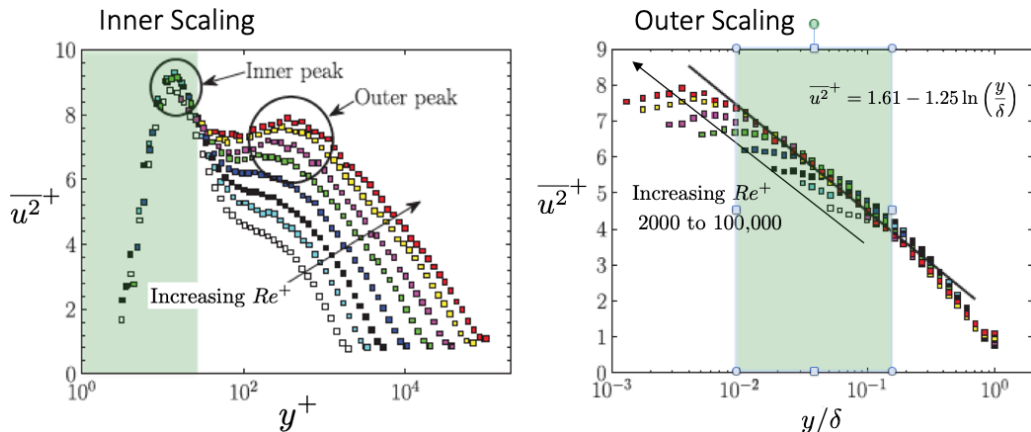


FIG. 12. Scaling of the streamwise turbulence component in pipe flow. Left: inner scaling. Right: outer scaling. Reproduction with permission from [65].

to the wall required a reliable spatial correction method, and so a correction method was developed based on AEM concepts [34] and applied to the NSTAP data. Bearing these considerations in mind, the streamwise turbulence intensity distributions measured in the Superpipe are shown in Fig. 12. In inner scaling [Fig. 12(a)], there are several notable features: the collapse of the data for y^+ less than about 20 with a prominent peak at about $y^+ = 15$, the orderly increase in the intensity levels in the outer layer, and the gradual emergence of a peak in the outer layer at large Reynolds numbers. Some of these features had been seen previously in boundary layers [27], but the outer peak was not seen in that investigation, most likely due to the limit on the maximum possible Reynolds numbers. The outer peak had been seen before by Morrison *et al.* [63], but there were legitimate reservations regarding those measurements due to their limited spatial resolution (see, for example, [64]).

For the data shown in Fig. 12, the most severe spatial resolution issues occur at the highest Reynolds numbers where $\ell^+ = 45.5$ (see Table II). As indicated above, the results were corrected using the scheme proposed by [34], which should be uncontroversial in the outer region where we see the outer peak; in other words, the peak is not an artifact of the measurement technique. This is not the case near the wall, however, where the Superpipe data suggest that the magnitude of the inner peak reaches an asymptotic level with increasing Reynolds number [16], which later studies seemed to confirm [61]. This view stood in contrast to other work, where the peak was believed to increase with Reynolds number, sometimes spectacularly so [66]. These disparate observations were not resolved until the recent work by Samie *et al.* [67], where NSTAP probes were used in a turbulent boundary layer about 300 mm thick to achieve measurements with $\ell^+ < 3.5$ for all

TABLE II. Experimental conditions for Superpipe turbulence experiments [65].

$Re_D = 2D\bar{U}/\nu$	Re^+	P (bar)	\bar{U} (m)	ℓ (μm)	ℓ^+ (m/s)	ℓ^+
81×10^3	1985	1.0	9.5	60	1.8	1.8
146×10^3	3334	1.7	10.1	60	3.1	1.8
247×10^3	5411	3.2	8.4	60	5.0	1.8
513×10^3	10481	6.4	9.4	60	9.7	1.8
1.1×10^6	20251	11.5	10.8	60	18.8	1.8
2.1×10^6	37450	23.4	10.5	30	17.4	1.8
4.0×10^6	68371	46.9	10.4	30	31.7	1.8
6.0×10^6	98187	70.7	10.6	30	45.5	1.8

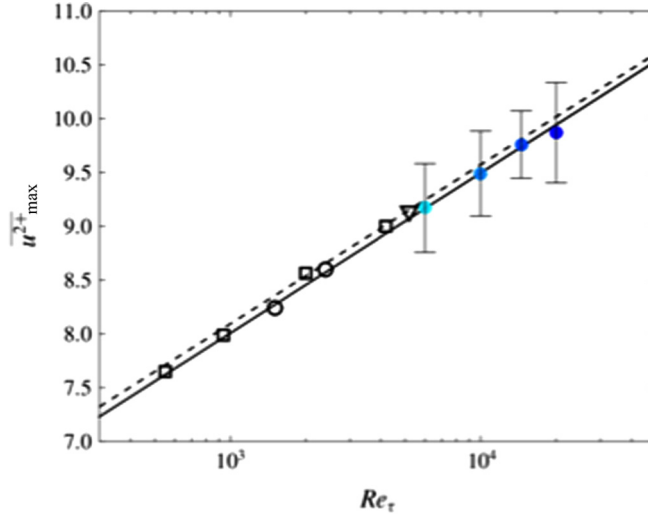


FIG. 13. Inner peak magnitude growth with Reynolds number. Dashed line is from DNS [68]. Solid line is $\overline{u^2}_{\max} = 3.54 + 0.646 \ln Re^+$ [Eq. (11)]. Reproduction with permission from [67].

Reynolds numbers. The data confirmed the presence of the outer peak, as well as establishing that in boundary layers the inner peak magnitude varied according to

$$\overline{u^2}_{\max} = 3.54 + 0.646 \ln Re^+, \quad (11)$$

in close agreement with the results obtained from DNS of channel flow by [68], as shown in Fig. 13.

In outer scaling [Fig. 12(b)], the data confirmed the presence of a logarithmic variation in the streamwise component, as predicted by the AEM. This experiment was the first to show this result, but it was quickly followed by results from high Reynolds number boundary layers that showed a similar behavior [69], as seen in Fig. 14. The boundary layer data obtained in the HRTF gave further confirmation of this trend, at Re^+ up to 73 000 [70]. What is more, it was found that the slope $A_1 = 1.26$ was the same for pipe and boundary layer flows, and it has been proposed to call it the Townsend-Perry constant in honor of the two AEM pioneers. This logarithmic variation appears to be universal for all (canonical) wall-bounded flows, although the additive constant B_1 seems to demonstrate a dependence on the flow geometry. The Reynolds number for the DNS results by Lee and Moser [68] was too low to show this logarithmic variation for the streamwise component; they did find a logarithmic variation for the spanwise component (as expected from the AEM), but intriguingly the logarithmic behavior for the wall-parallel component seems to emerge at a lower Reynolds number than that for the streamwise component, a result that has not yet been verified by experiment.

The logarithmic variation for the streamwise component is also seen in rough pipes with small relative roughness (see [71]), which is also a result that is expected from the AEM. Interestingly, even the higher order moments follow a logarithmic behavior, as illustrated in Fig. 15 for the fourth-order moment. If the turbulence was Gaussian, the expected slope for the fourth-order moment would be $1.26\sqrt{3} = 2.18$, while the measured slope is reasonably close at about 2, for smooth and rough pipe flows (Fig. 15). A closer examination of the higher order moments is given by [70,72].

These results represent major successes for the AEM. However, some questions remain. The AEM assumes that the region very near the wall is additive to the attached eddies. Since the extent of the logarithmic region grows with Reynolds number, this implies that the (log) magnitude of the peak will increase at the rate given by $A_1 = 1.26$. The data, however, show a variation that is about half this rate [Eq. (11), Fig. 13]. This remains an open question that deserves further study.

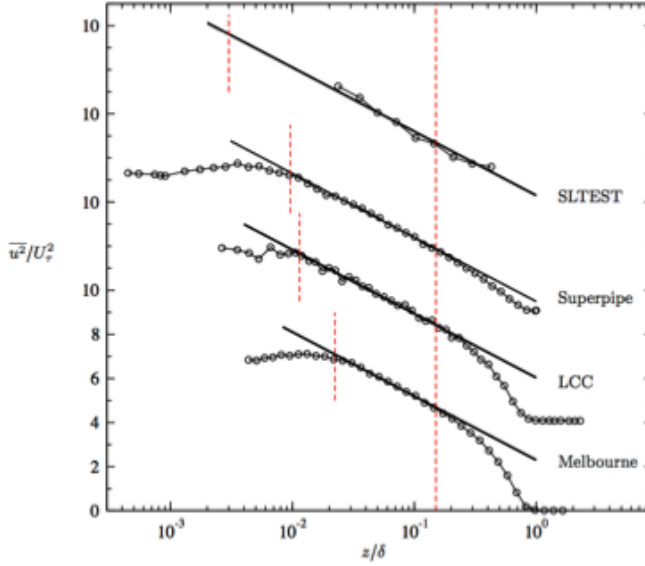


FIG. 14. A universal log law for turbulence? Streamwise turbulence intensity: Melbourne wind tunnel $Re_\tau = 18\,010$ ($2.5\ \mu\text{m}$ hot wire); Large Cavitation Channel $Re_\tau = 68\,780$ (LDV); Princeton Superpipe $Re_\tau = 98\,190$ (NSTAP); SLTEST $Re_\tau \approx 628\,000$ (Sonics). The solid straight lines correspond to Eq. (3) with $A_1 = 1.26$. Reproduction with permission from [69].

In Fig. 16 we show the results for the pipe flow (Superpipe) and the turbulent boundary layer (HRTF) at their respective maximum Reynolds number where turbulence data were obtained. It is apparent that the region of logarithmic similarity occupies the same physical region in space, although the beginning and end points of the logarithmic regions are somewhat different, and their

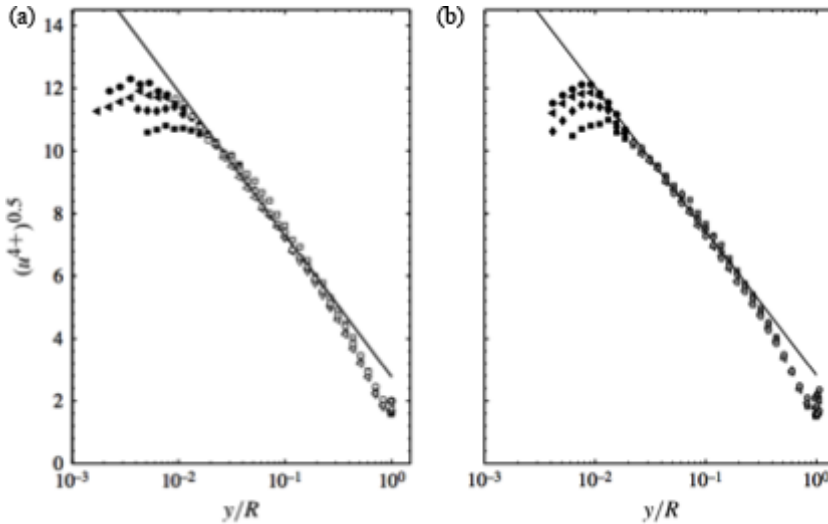


FIG. 15. A universal log law for turbulence? Outer scaled streamwise Reynolds stress profiles of four highest Reynolds numbers of (a) smooth- and (b) rough-wall Superpipe datasets. The solid line has a slope of -2.0 . The Gaussian expectation for the slope is $1.26\sqrt{3} = -2.18$. Reproduction with permission from [71].

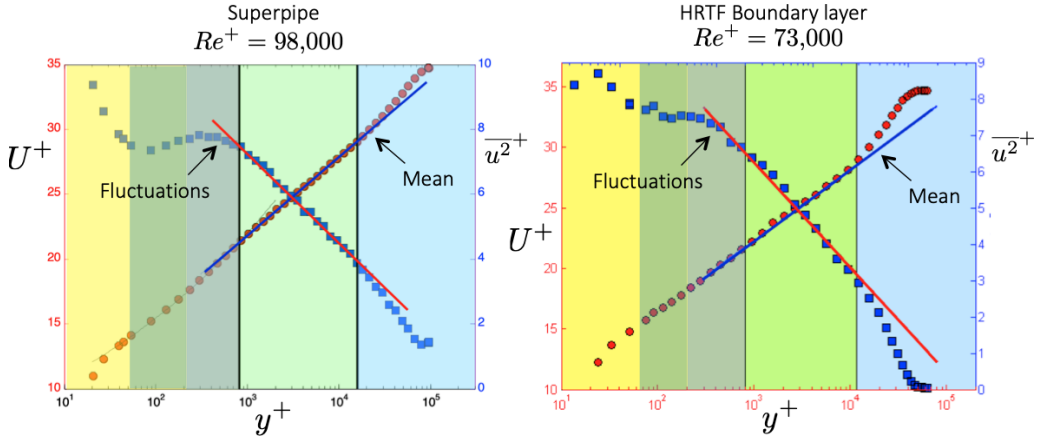


FIG. 16. Scaling in the equilibrium region. Left: pipe flow at $Re_\tau = 98\,000$. Right: boundary layer flow at $Re_\tau = 73\,000$. Reproduction with permission from [70,71]. The grey region marks the mesolayer.

exact location in inner and outer coordinates is still the subject of current research. In this respect [37,73], present additional analysis and considerations.

Also seen in this figure is a grey region, extending from about $y^+ = 67$ in the pipe and $y^+ = 50$ in the boundary layer, lying between the buffer layer where inner scaling applies, and the logarithmic layer where the flow is free of viscous effects. In the grey region, a Reynolds number dependent behavior can be seen in all parameters, which we identify as the mesolayer. The mesolayer has been the subject of considerable attention in the past (see, for example, [74–76], but the lower bounds found here are somewhat different. In this region, we find that the turbulence intensity is almost constant at lower Reynolds numbers while it is slightly rising at higher Reynolds numbers. In the mean velocity, the profile follows a power law in y^+ .

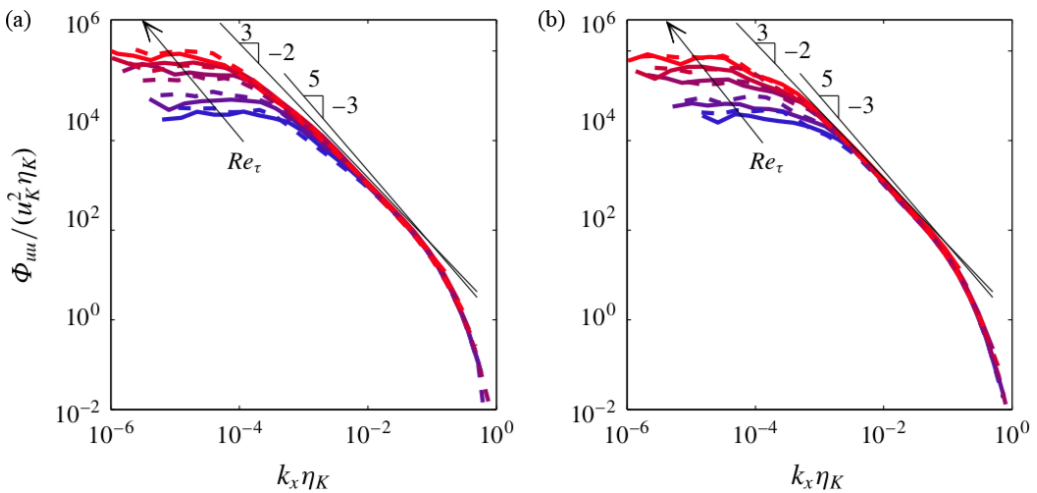


FIG. 17. Kolmogorov spectra for $Re_\tau \approx 3 \times 10^3, 5 \times 10^3, 10 \times 10^3, 20 \times 10^3, 40 \times 10^3,$ and 70×10^3 , at $y/\delta \approx 0.05$ (left) and $y/\delta \approx 0.5$ (right). —, boundary layer; ---, pipe. Reproduction with permission from [77].

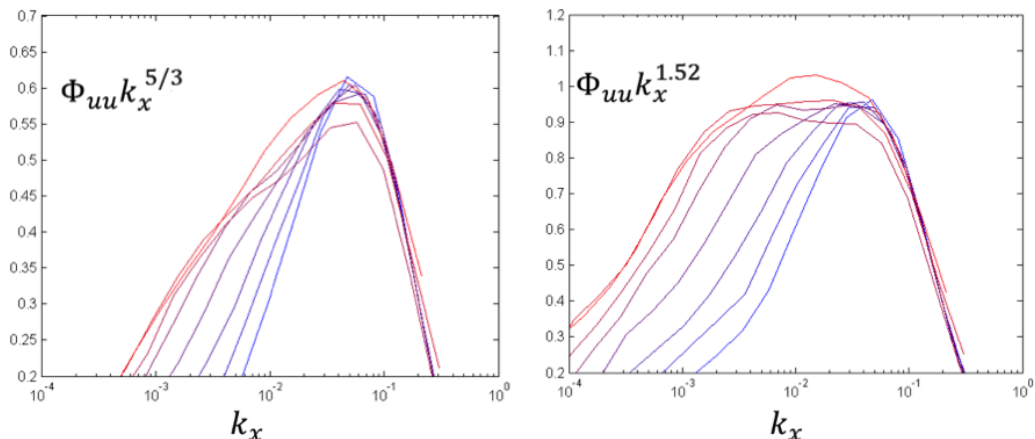


FIG. 18. Premultiplied spectra at $y/\delta = 0.1$ in pipe for $2000 \leq \text{Re}_\tau \leq 98\,000$. Colors go from blue to red as the Reynolds number increases. Left: premultiplied by $k_1^{5/3}$. Right: premultiplied by $k_1^{1.52}$. Reproduction with permission from [77].

VI. RESULTS ON THE SPECTRUM

Here, we only consider the one-dimensional spectrum of the streamwise component of the turbulence, that is, $\phi_{11}(k_1)$. We noted earlier that Perry and Abell [57] proposed that, at sufficiently high Reynolds numbers, there may exist overlap regions between the $R - y$ regions, and between the $y - \eta$ regions, which yield a k^{-1} region and a $k^{-5/3}$ Kolmogorov region (see also Perry *et al.* [58]).

We first consider the presence of a $-5/3$ region. The spectrum in Kolmogorov scaling is shown in Fig. 17 for the pipe and boundary layer flows, as measured in the Superpipe and the HRTF [77] at two positions, one within the logarithmic region. At high wave numbers, the spectra collapse well in this scaling, but the inertial region does not follow a $k_1^{-5/3}$ slope. This is more clearly seen in the premultiplied spectra shown in Fig. 18. Multiplication by the correct prefactor (that is, the best fit to the slope in log-log coordinates) should reveal a plateau region. It is apparent that the exponent of -1.52 is a better fit to the data than $-5/3$, which is in accordance with the observations by Gamard and George [78], as given in Fig. 19. The Reynolds number here is given by $R_\lambda = \lambda u_{\text{rms}}/\nu$, where λ is the Taylor microscale. For the highest Reynolds numbers in the pipe and boundary layer, $R_\lambda \approx 1000$ at $y/\delta = 0.1$ [79], and so a value of 1.52 of the exponent fits in well with these earlier experiments and the theory of [78]. This plot also makes clear that the exponent of $-5/3$ will only be

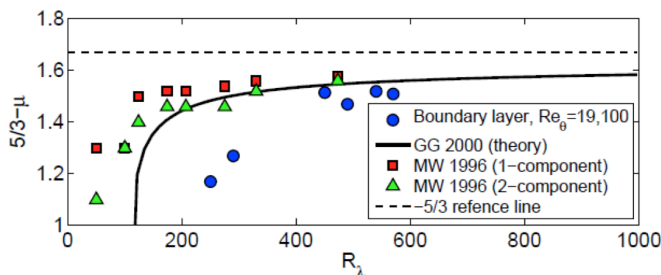


FIG. 19. Inertial layer slope. Here, $\Phi_{uu} \sim k_x^{-5/3 + \mu}$, where $\mu \sim \ln^{-1} \text{Re}$. Data marked MW are from [80], theory marked GG is from [78]. Reproduction with permission from [81].

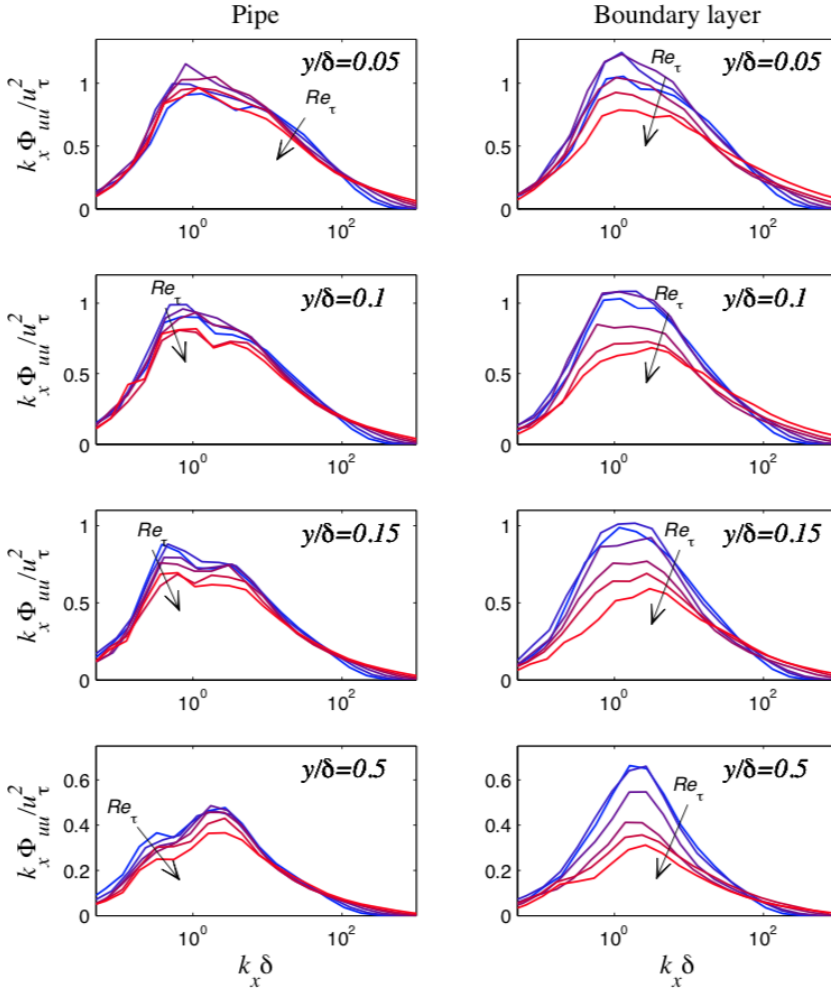


FIG. 20. Premultiplied spectra with varying Reynolds number at fixed wall-normal locations $y/\delta \approx 0.05, 0.1, 0.15, 0.5$ for pipe (left) and boundary layer (right). Arrows indicate the increasing Reynolds number from $Re^+ = 3000$ to $Re^+ = 70000$. The region of k_x^{-1} should appear as a plateau. Reproduction with permission from [77].

reached at extremely high Reynolds numbers, well outside even the values obtained in the Superpipe and HRTF experiments.

Consider now the presence of a -1 region. The premultiplied form of the spectrum is shown in outer scaling in Fig. 20 for the pipe and boundary layer flows, as measured in the Superpipe and the HRTF [77] at a number of different positions. In this representation (multiplication by k_1), the spectrum is expected to show a constant plateau in the k_1^{-1} region, with an amplitude of A_1 , as discussed earlier. However, for neither the pipe nor the boundary layer, no matter what the Reynolds number is or what the position within the layer is, do we see a clear plateau region. As concluded by Vallikivi *et al.* [77], it appears that in boundary layer and pipe flows in the turbulent wall region there is no obvious k^{-1} region that persists with Reynolds number, or with a change in wall-normal location, and the spectra do not exhibit a region that collapses both in inner and outer scaling. This brings into question the relationship between the spectral overlap arguments of Perry and Abell [57] and Perry *et al.* (1986) [58] and the logarithmic variation of the variances.

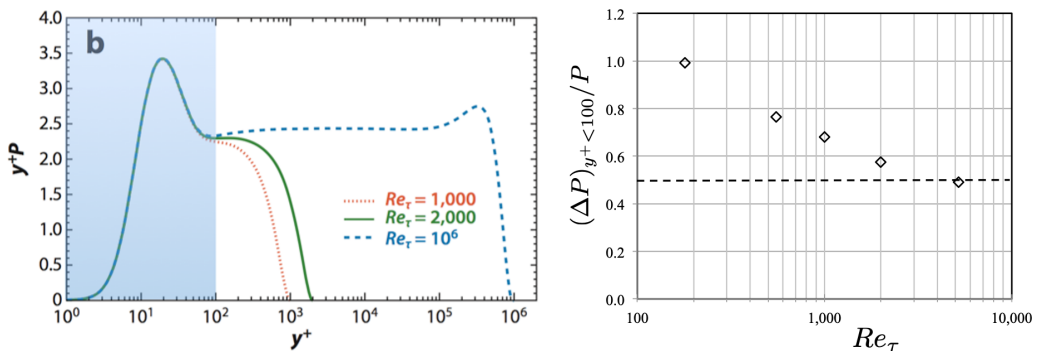


FIG. 21. Turbulence kinetic energy production. Left: premultiplied form, where equal areas represent equal contributions to the total production. Adapted with permission from [37]. Right: fraction of total production contributed by the region for $y^+ \leq 100$ (data from [68]).

VII. LARGE-SCALE MOTIONS

As was evident from the spectra shown in Fig. 17, the fraction of the total energy contained in the large-scale motions increases with Reynolds number. See also Fig. 2 in [37]. Another indication of the increasing role played by the large-scale motions is given by the turbulence production term in the Reynolds-averaged Navier-Stokes (RANS) equations. The variation of the production term with distance from the wall is shown in Fig. 21 in premultiplied form, where equal areas represent equal contributions to the total production. On the left, we see that the near-wall contribution (for $y^+ < 100$) dominates the total production at low Reynolds number, but as the Reynolds number increases the outer region contribution becomes more and more important. On the right in Fig. 21, the fractional contribution of the near-wall production to the total production is plotted as a function of Reynolds number for the DNS data of Lee and Moser [68]. At about $Re_\tau = 5000$ the contribution from the outer layer exceeds the contribution from the inner layer. Hence large-scale motions that contribute to the equilibrium region (LSM) and the outer region (VLSM) eventually come to dominate the production at higher Reynolds numbers. This trend was seen already by [40], who observed a growing contribution to the energy spectrum from motions with length scales of $O(10R)$ with Reynolds number; the first recorded observation of the VLSM in turbulent wall-bounded flows. See also [38,82,83].

Experiments to gain more insight into the organized motions within high-pressure facilities like the Superpipe and HRTF can be challenging. Measurements using multiple hot wires are certainly possible [84], but they can provide only limited data on structure. Particle image velocimetry (PIV) data are much more informative, in that they can give spatial information in two or three dimensions, but optical access to the flow is often difficult to achieve. We are now modifying the Superpipe working section to allow such optical access for PIV, but a great deal has already been learned from measurements at lower Reynolds numbers in a pipe facility that uses water as the working fluid. In particular, proper orthogonal decomposition (POD) and spectral analysis of PIV data have proved to be powerful tools for investigating the nature of the LSM and VLSM [85–90].

According to Hellström and Smits [86], the POD modes ranked by energy content come in pairs, and the first five pairs contain 15% of the total energy and 43% of the integrated Reynolds shear stress even at $Re^+ = 2260$, and so POD modes might serve well as a low-order representation for the momentum transfer. Somewhat surprisingly, the first 80 modes all give positive contributions to $-\overline{uv}$ (see Fig. 22). In addition, the VLSM are well represented by a small number of the most energetic POD modes, as illustrated in Fig. 23. Note especially the long, meandering structure in the lower right corner of the image, and how its structure is well captured by the just first four most energetic modes.

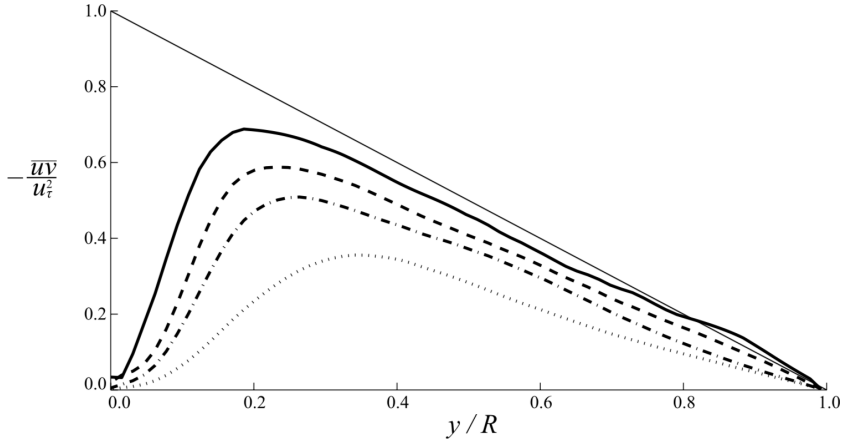


FIG. 22. Contributions to the Reynolds shear stress at $\text{Re}_D = 93\,000$ ($\text{Re}^+ = 2260$). Bold lines show the shear stress contained in the reconstructed flow, using $\cdot\cdot\cdot\cdot$, 10; $\cdot-\cdot-$, 30; $---$, 80 snapshot POD modes; $---$, all modes. The straight line indicates the distribution of the total shear stress. Reproduction with permission from [86].

To examine the structure of these modes, we sort them in terms of their radial (n) and azimuthal (m) modes. The most energetic modes are those with $m = 3$, followed by $m = 2$ and $m = 4$, all having one radial structure $n = 1$ [86]. For $n > 1$ the modes begin to represent detached motions. As illustrated in Fig. 24, it is apparent that as m and n increase, the modes contribute more and more to the near-wall energy, with only a weak Reynolds number dependence. Also, the peak energies for the first four azimuthal modes ($m = 1$ to 4) are located at a frequency of $fD/U = 0.05$ to 0.1, corresponding to structures $10D$ to $20D$ long, clearly indicative of the VLSM.

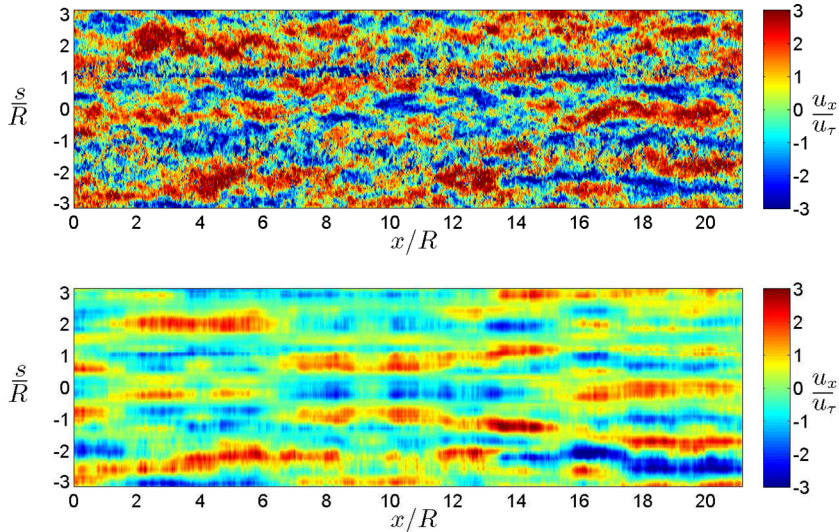


FIG. 23. Contour plots of the streamwise velocity fluctuations at $y/R = 0.2$ and $\text{Re}_D = 12\,500$, constructed using Taylor's hypothesis. Flow is from left to right. Top: instantaneous fluctuations. Bottom: superposition of the first four POD modes, showing how long, meandering structures can be formed from a small number of modes. Adapted with permission from [85].

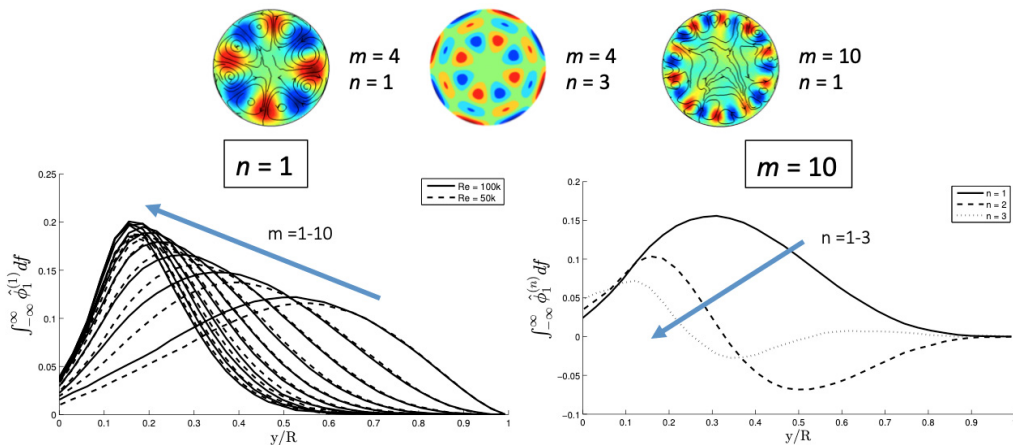


FIG. 24. The radial behavior of the classical POD modes, averaged over all frequencies. Left: Azimuthal modes $m = 1-10$ for the first POD mode, $n = 1$. ---, $Re_D = 47\,000$ ($Re^+ = 1210$); —, $Re_D = 93\,000$ ($Re^+ = 2260$). Right: POD modes for $m = 3$ and —, $n = 1$; ---, $n = 2$; and \cdots , $n = 3$. Adapted with permission from [86].

To investigate the origin of the VLSM, Hellström *et al.* [87] acquired PIV data simultaneously in a cross-stream plane and in a streamwise plane on the pipe centerline. The most energetic POD modes, the ones associated with the VLSM, were found to have a characteristic streamwise extent of $\approx 3R$ (see [91]), after which a transition to a new structure occurs that is marked by the detachment and decay of an old structure and the initiation of a new structure at the wall. These modes appear to describe a basic building block similar to that of the LSM, and that these blocks line up to create a longer structure with a typical length estimated to about $6R$. It was also shown that the structure described by a specific azimuthal mode number, m , was azimuthally steady. The meandering nature of the VLSM is likely a consequence of the interaction between structures with different azimuthal mode numbers. It was therefore proposed that the coherence of the long meandering structures visualized by multipoint measurements is actually the consequence of a pseudoalignment of shorter modes/structures, combined with the reoccurrence of a specific mode/structure at regular time intervals. The shorter structures appear to have characteristics very similar to LSM, and these support the suggestions by [40] and [92] that the VLSM are in fact not spatial structures but a temporal manifestation of repeating LSM.

Furthermore, the POD modes display self-similarity in accordance with the AEM, in they scale with the distance from the wall [88]. The modes resolving the energetic eddies in the homogeneous directions are the harmonic ones, and thus they are inherently self-similar. It was also found that, in the wave number range $k_\theta R \in [4.16, 33.3]$ (almost a decade), the only nonhomogeneous directions also are self-similar, and all eddies can be fully described with a single radial profile (see Fig. 25). The length scale representing the eddy could be estimated by its wall-normal radius, which is a universal length scale completely describing the cross-sectional shape of the structure through all stages of its evolution. It was recently shown that the wall-normal length scale is also the appropriate streamwise length scale, so that the structures showed complete similarity [90].

VIII. CONCLUSIONS AND SOME OBSERVATIONS

The concept of wall-attached eddies that scale with the distance from the wall, as embodied in the attached eddy model, is undoubtedly a powerful organizing concept for the all-important equilibrium region of wall-bounded turbulence. Our measurements over a wide range of Reynolds numbers have confirmed many aspects of the attached eddy model. Modal analysis revealed a

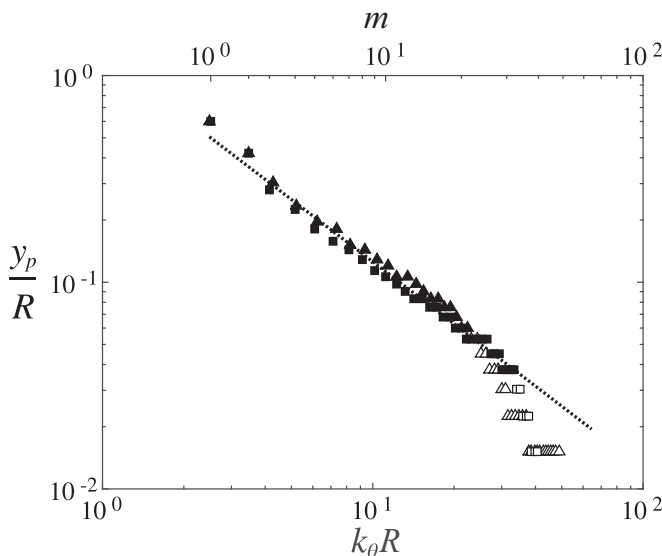


FIG. 25. Modal peak location for the first POD mode ($n = 1$) and azimuthal mode numbers $m \in [1, 64]$. \blacktriangle $\text{Re}^+ = 1330$; \blacksquare $\text{Re}^+ = 2460$; \cdots $y_p/R = 2\pi C (k_\theta R)^{-1}$, with $C = 0.2$. Modes with a peak location $y_p^+ < 75$ are identified with open symbols. The lower abscissa indicates the azimuthal wave number, while the upper abscissa shows the corresponding azimuthal mode number, for $\text{Re}^+ = 2460$. Reproduction with permission from [88].

complete self-similarity for the attached eddy structure in a pipe, and the presence of a log law in turbulence has been shown to occur in the same region where the log law in mean velocity is found, but only for $\text{Re}^+ > 10\,000$. It is now clear that viscous effects remain important for large distances from the wall, so that the predictions from the AEM and other similarity arguments will only work at distances from the wall greater than about ten times the viscous sublayer and buffer layer thicknesses combined. We see the mesolayer as the blending region between the viscous scaling and the outer scaling for both the mean velocity and the turbulence, although it only becomes evident at a sufficiently high Reynolds number.

Nevertheless, some of our results cannot as yet be reconciled with the AEM. For example, the inner peak in the streamwise turbulence increases logarithmically with Re^+ , but at a rate that is much slower than expected from the AEM. An outer peak in the turbulence intensity appears for $\text{Re}^+ > 10\,000$, and its origin remains to be explained. Also, spectral data point to the elusiveness of any possible asymptotic behavior with increasing Reynolds number. For example, the slope of the inertial region asymptotes very slowly to $-5/3$, and no k^{-1} region was found at the Reynolds numbers reported here. The spectral overlap arguments that support the -1 region are independent of the AEM, but they share with the AEM the scaling of the wall motions with distance from the wall, and the scaling of the larger motions with the layer thickness. Some adjustments will be necessary to make the two points of view come into better agreement. It may be that the increasing dominance of the VLSM may be disrupting the AEM at higher Reynolds number, but this will need to be investigated further.

I would like to end with a word of caution, and some suggestions for future work. We have learned a lot by studying pipes, boundary layers, and channels, and there are still gaps in our knowledge. Such flows are canonical but they are also singular, in that they are two-dimensional in the mean, and the smallest departure from, for example, zero pressure gradient or the flatness condition leads to significant changes in all aspects of the mean flow and the turbulence. Flows over vehicles, or within ducting systems, experience the effects of roughness, pressure gradients,

surface curvature, three-dimensionality, separation, blowing, suction, etc. We therefore need to move beyond canonical flows, not just to address practical applications but also to learn what parts of our understanding of canonical flows survive under such perturbations. I would suggest, in fact, that we may have reached a point of diminishing returns in studying canonical flows. It may be more fruitful to begin to test our knowledge of wall-bounded flows by examining more complicated flows. We might ask the question “Do we have enough insight into the structure of wall-bounded flows to manipulate the energetic motions and reduce drag, or enhance heat transfer?” Or, “What fundamental understanding might we gain by such experiments?” Many other problems can be posed along these lines, and I believe that such investigations will undoubtedly lead to a deeper and more nuanced understanding of wall turbulence, while expanding our abilities to predict more general flow behavior.

ACKNOWLEDGMENTS

This work was supported by ONR under Grants No. N00014-17-1-2309 and No. N00014-19-1-2301. Dr. Liuyang Ding kindly provided comments on an earlier draft.

-
- [1] H. L. Grant, R. W. Stewart, and A. Moilliet, Turbulence spectra from a tidal channel, *J. Fluid Mech.* **12**, 241 (1962).
 - [2] R. J. Taylor, A new approach to the measurement of turbulent fluxes in the lower atmosphere, *J. Fluid Mech.* **10**, 449 (1961).
 - [3] G. I. Taylor, Eddy motion in the atmosphere, *Philos. Trans. R. Soc. London A* **215**, 1 (1915).
 - [4] M. M. Munk, On a new type of wind tunnel, NACA Technical Note 60, 1921 (unpublished).
 - [5] M. M. Munk and E. W. Miller, The Variable Density Wind Tunnel of the National Advisory Committee for Aeronautics, NACA Technical Report 227, 1927 (unpublished).
 - [6] E. N. Jacobs and I. H. Abbott, The N.A.C.A. Variable Density Wind Tunnel, NACA Technical Report 416, 1933 (unpublished).
 - [7] A. E. Von Doenhoff and F. T. Abbott, The Langley two-dimensional Low-Turbulence Pressure Tunnel, NACA Technical Note 1283, 1947 (unpublished).
 - [8] E. F. Relf, Modern developments in the design of aeroplanes, *J. Inst. Civil Eng.* **3**, 523 (1936).
 - [9] C. B. Millikan, J. E. Smith, and R. W. Bell, High-speed testing in the southern california cooperative wind tunnel, *J. Aeronaut. Sci.* **15**, 69 (1948).
 - [10] E. Achenbach, Experiments on the flow past spheres at very high Reynolds numbers, *J. Fluid Mech.* **54**, 565 (1972).
 - [11] A. Spence, D. S. Woodward, M. T. Caiger, A. J. Sadler, and R. W. Jeffery, The RAE 5 metre pressurized low speed wind tunnel, in *11th ICAS Congress*, Lisbon, 1978 (ICAS, Bonn, 1978), pp. 11–16.
 - [12] J. M. Carrara and A. Masson, Three years of operation of the ONERA pressurized subsonic wind tunnel, in *12th ICAS Congress*, Munich, 1980 (ICAS, Bonn, 1980), pp. 780–792.
 - [13] H. Försching, E. Melzer, and G. Schewe, Ein neuer Windkanal für gebäudeaerodynamische und-aeroelastische Untersuchungen bei Reynoldszahlen bis 10^7 , DFVLR-AVA Technical Report IB 232-81 J 02, 1981 (unpublished).
 - [14] M. V. Zagarola, Mean-flow scaling of turbulent pipe flow, Ph.D. thesis, Princeton University, 1996 (unpublished).
 - [15] D. B. DeGraaff, The scaling of the turbulent boundary layer on a flat plate and on swept and unswept bumps, Ph.D. thesis, Stanford University, Stanford, CA, 1999 (unpublished).
 - [16] M. Hultmark, S. C. C. Bailey, and A. J. Smits, Scaling of near-wall turbulence in pipe flow, *J. Fluid Mech.* **649**, 103 (2010).
 - [17] E. Bodenschatz, G. P. Bewley, H. Nobach, M. Sinhuber, and H. Xu, Variable density turbulence tunnel facility, *Rev. Sci. Instrum.* **85**, 093908 (2014).

- [18] K. Steiros and M. Hultmark, Princeton high Reynolds number Supertank facility, *Bull. Am. Phys. Soc.* **72**, (2019).
- [19] R. C. Pankhurst, Aerodynamics at NPL, 1917–1970, *Nature (London)* **238**, 375 (1972).
- [20] A. L. Kistler and T. Vrebalovich, Grid turbulence at large Reynolds numbers, *J. Fluid Mech.* **26**, 37 (1966).
- [21] G. Schewe, Nonlinear flow-induced resonances of an H-shaped section, *J. Fluids Struct.* **3**, 327 (1989).
- [22] G. Schewe, On the force fluctuations acting on a circular cylinder in crossflow from subcritical up to transcritical Reynolds numbers, *J. Fluid Mech.* **133**, 265 (1983).
- [23] G. Schewe, Reynolds-number effects in flow around more-or-less bluff bodies, *J. Wind Eng. Ind. Aerodyn.* **89**, 1267 (2001).
- [24] E. Llorente, A. Gorostidi, M. Jacobs, W. A. Timmer, X. Munduate, and O. Pires, Wind tunnel tests of wind turbine airfoils at high Reynolds numbers, *J. Phys.: Conf. Ser.* **524**, 012012 (2014).
- [25] A. J. Smits, New approaches to experimental turbulence research, AFOSR Technical Report AD-A243 989, 1991 (unpublished).
- [26] M. V. Zagarola, A. J. Smits, G. L. Brown, S. A. Orszag, and V. Yakhot, Superpipe: A high Reynolds number turbulence experiment, *Bull. Am. Phys. Soc.* **45**, (1992).
- [27] D. B. DeGraaff and J. K. Eaton, Reynolds-number scaling of the flat-plate turbulent boundary layer, *J. Fluid Mech.* **422**, 319 (2000).
- [28] M. Fu and M. Hultmark (private communication).
- [29] A. A. Townsend, *The Structure of Turbulent Shear Flow* (Cambridge University Press, Cambridge, UK, 1976).
- [30] A. E. Perry and M. S. Chong, On the mechanism of wall turbulence, *J. Fluid Mech.* **119**, 173 (1982).
- [31] B. J. McKeon and A. S. Sharma, A critical layer framework for turbulent pipe flow, *J. Fluid Mech.* **658**, 336 (2010).
- [32] P. A. Monkewitz and H. M. Nagib, Large-Reynolds-number asymptotics of the streamwise normal stress in zero-pressure-gradient turbulent boundary layers, *J. Fluid Mech.* **783**, 474 (2015).
- [33] K. Taira, S. L. Brunton, S. T. M. Dawson, C. W. Rowley, T. Colonius, B. J. McKeon, O. T. Schmidt, S. Gordeyev, V. Theofilis, and L. S. Ukeiley, Modal analysis of fluid flows: An overview, *AIAA J.* **55**, 4013 (2017).
- [34] A. J. Smits, J. Monty, M. Hultmark, S. C. C. Bailey, M. Hutchins, and I. Marusic, Spatial resolution correction for turbulence measurements, *J. Fluid Mech.* **676**, 41 (2011).
- [35] C. J. Delo, Volumetric analysis of a low Reynolds number turbulent boundary layer, Ph.D. thesis, Princeton University, Princeton, NJ, USA, 1996 (unpublished).
- [36] M. Van Dyke, *An Album of Fluid Motion* (Parabolic, Stanford, 1982).
- [37] A. J. Smits, B. J. McKeon, and I. Marusic, High Reynolds number wall turbulence, *Annu. Rev. Fluid Mech.* **43**, 353 (2011).
- [38] J. P. Monty, J. A. Stewart, R. C. Williams, and M. S. Chong, Large-scale features in turbulent pipe and channel flows, *J. Fluid Mech.* **589**, 147 (2007).
- [39] K. Kevin, J. P. Monty, and N. Hutchins, The meandering behaviour of large-scale structures in turbulent boundary layers, *J. Fluid Mech.* **865**, R1 (2019).
- [40] K. C. Kim and R. J. Adrian, Very large-scale motion in the outer layer, *Phys. Fluids* **11**, 417 (1999).
- [41] B. J. Cantwell, D. E. Coles, and P. Dimotakis, Structure and entrainment in the plane of symmetry of a turbulent spot, *J. Fluid Mech.* **87**, 641 (1978).
- [42] T. Theodorsen, The structure of turbulence, in *50 Jahre Grenzschichtforschung* (Springer, Berlin, 1955), pp. 55–62.
- [43] M. R. Head and P. Bandyopadhyay, New aspects of turbulent boundary-layer structure, *J. Fluid Mech.* **107**, 297 (1981).
- [44] R. J. Adrian, C. D. Meinhart, and C. D. Tomkins, Vortex organization in the outer region of the turbulent boundary layer, *J. Fluid Mech.* **422**, 1 (2000).
- [45] N. Hutchins and I. Marusic, Evidence of very long meandering streamwise structures in the logarithmic region of turbulent boundary layers, *J. Fluid Mech.* **579**, 1 (2007).

- [46] C. B. Millikan, A critical discussion of turbulent flows in channels and circular tubes, in *Proceedings of the fifth International Congress for Applied Mechanics*, Cambridge, MA, 1938 (John Wiley & Sons, New York, 1939).
- [47] B. J. McKeon, J. Li, W. Jiang, J. F. Morrison, and A. J. Smits, Further observations on the mean velocity distribution in fully developed pipe flow, *J. Fluid Mech.* **501**, 135 (2004).
- [48] H. M. Nagib, K. A. Chauhan, and P. A. Monkewitz, Approach to an asymptotic state for zero pressure gradient turbulent boundary layers, *Philos. Trans. R. Soc. London A* **365**, 755 (2007).
- [49] V. C. Patel, Calibration of the Preston tube and limitations on its use in pressure gradients, *J. Fluid Mech.* **23**, 185 (1965).
- [50] S. C. C. Bailey, M. Vallikivi, M. Hultmark, and A. J. Smits, Estimating the value of von Kármán's constant in turbulent pipe flow, *J. Fluid Mech.* **749**, 79 (2014).
- [51] M. V. Zagarola and A. J. Smits, Mean-flow scaling of turbulent pipe flow, *J. Fluid Mech.* **373**, 33 (1998).
- [52] M. V. Zagarola and A. J. Smits, A new mean velocity scaling for turbulent boundary layers, in *Proceedings of FEDSM'98*, Washington, DC, 1998, paper FEDSM98-4950 (ASME, New York, 1998).
- [53] R. B. Cal and L. Castillo, Scaling turbulent boundary layer with suction or blowing, in *IUTAM Symposium on Reynolds Number Scaling in Turbulent Flow* (Springer, Berlin, 2004), pp. 195–199.
- [54] L. Castillo and W. K. George, Similarity analysis for turbulent boundary layer with pressure gradient: Outer flow, *AIAA J.* **39**, 41 (2001).
- [55] T. Theodorsen, Mechanism of turbulence, in *Proceedings of the Second Midwestern Conference on Fluid Mechanics*, Columbus, OH, 1952 (College of Engineering, Ohio State University, Columbus 1952).
- [56] I. Marusic and J. P. Monty, Attached eddy model of wall turbulence, *Annu. Rev. Fluid Mech.* **51**, 49 (2019).
- [57] A. E. Perry and C. J. Abell, Asymptotic similarity of turbulence structures in smooth- and rough-walled pipes, *J. Fluid Mech.* **79**, 785 (1977).
- [58] A. E. Perry, S. M. Henbest, and M. S. Chong, A theoretical and experimental study of wall turbulence, *J. Fluid Mech.* **165**, 163 (1986).
- [59] I. Marusic, M. Uddin, and A. E. Perry, Similarity law for the streamwise turbulence intensity in zero-pressure-gradient turbulent boundary layers, *Phys. Fluids* **12**, 3718 (1997).
- [60] S. C. C. Bailey, G. J. Kunkel, M. Hultmark, M. Vallikivi, J. P. Hill, K. A. Meyer, C. Tsay, C. B. Arnold, and A. J. Smits, Turbulence measurements using a nanoscale thermal anemometry probe, *J. Fluid Mech.* **663**, 160 (2010).
- [61] M. Vallikivi, M. Hultmark, S. C. C. Bailey, and A. J. Smits, Turbulence measurements in pipe flow using a nano-scale thermal anemometry probe, *Exp. Fluids* **51**, 1521 (2011).
- [62] M. Vallikivi and A. J. Smits, Fabrication and characterization of a novel nano-scale thermal anemometry probe, *J. Microelectromech. Syst.* **23**, 899 (2014).
- [63] J. F. Morrison, B. J. McKeon, W. Jiang, and A. J. Smits, Scaling of the streamwise velocity component in turbulent pipe flow, *J. Fluid Mech.* **508**, 99 (2004).
- [64] N. Hutchins, T. B. Nickels, I. Marusic, and M. S. Chong, Hot-wire spatial resolution issues in wall-bounded turbulence, *J. Fluid Mech.* **635**, 103 (2009).
- [65] M. Hultmark, M. Vallikivi, S. C. C. Bailey, and A. J. Smits, Turbulent Pipe Flow at Extreme Reynolds Numbers, *Phys. Rev. Lett.* **108**, 094501 (2012).
- [66] I. Marusic and G. J. Kunkel, Streamwise turbulence intensity formulation for flat-plate boundary layers, *Phys. Fluids* **15**, 2461 (2003).
- [67] M. Samie, I. Marusic, N. Hutchins, M. K. Fu, Y. Fan, M. Hultmark, and A. J. Smits, Fully resolved measurements of turbulent boundary layer flows up to $Re_\tau = 20,000$, *J. Fluid Mech.* **851**, 391 (2018).
- [68] M. Lee and R. D. Moser, Direct numerical simulation of turbulent channel flow up to $Re_\tau = 5200$, *J. Fluid Mech.* **774**, 395 (2015).
- [69] I. Marusic, J. P. Monty, M. Hultmark, and A. J. Smits, On the logarithmic region in wall turbulence, *J. Fluid Mech.* **716**, R3 (2013).
- [70] M. Vallikivi, M. Hultmark, and A. J. Smits, Turbulent boundary layer statistics at very high Reynolds number, *J. Fluid Mech.* **779**, 371 (2015).

- [71] M. Hultmark, M. Vallikivi, S. C. C. Bailey, and A. J. Smits, Logarithmic scaling of turbulence in smooth- and rough-wall pipe flow, *J. Fluid Mech.* **728**, 376 (2013).
- [72] C. Meneveau and I. Marusic, Generalized logarithmic law for high-order moments in turbulent boundary layers, *J. Fluid Mech.* **719**, R1 (2013).
- [73] P. Fife, T. Wei, J. Klewicki, and P. McMurtry, Stress gradient balance layers and scale hierarchies in wall-bounded turbulent flows, *J. Fluid Mech.* **532**, 165 (2005).
- [74] N. Afzal, Fully developed turbulent flow in a pipe: An intermediate layer, *Ing.-Arch.* **52**, 355 (1982).
- [75] K. R. Sreenivasan and A. Sahay, The persistence of viscous effects in the overlap region and the mean velocity in turbulent pipe and channel flows, in *Self-Sustaining Mechanisms of Wall Turbulence*, edited by R. Panton (Computational Mechanics, Southampton, UK, 1997), pp. 253–272.
- [76] W. K. George and L. Castillo, Zero-pressure-gradient turbulent boundary layer, *Appl. Mech. Rev.* **50**, 689 (1997).
- [77] M. Vallikivi, B. Ganapathisubramani, and A. J. Smits, Spectral scaling in boundary layers and pipes at very high Reynolds numbers, *J. Fluid Mech.* **771**, 303 (2015).
- [78] S. Gamard and W. K. George, Reynolds number dependence of energy spectra in the overlap region of isotropic turbulence, *Flow, Turbul. Combust.* **63**, 443 (2000).
- [79] J. F. Morrison, M. Vallikivi, and A. J. Smits, The inertial subrange in turbulent pipe flow: Centreline, *J. Fluid Mech.* **788**, 602 (2016).
- [80] L. Mydlarski and Z. Warhaft, On the onset of high-Reynolds-number grid-generated wind tunnel turbulence, *J. Fluid Mech.* **320**, 331 (1996).
- [81] W. K. George and M. Tutkun, The mesolayer and reynolds number dependencies of boundary layer turbulence, in *Progress in Wall Turbulence: Understanding and Modeling*, edited by M. Stanislas, J. Jimenez, and I. Marusic (Springer, Dordrecht, 2011), pp. 183–190.
- [82] M. Guala, S. E. Hommea, and R. J. Adrian, Large-scale and very-large-scale motions in turbulent pipe flow, *J. Fluid Mech.* **554**, 521 (2006).
- [83] B. J. Balakumar and R. J. Adrian, Large- and very-large-scale motions in channel and boundary-layer flows, *Philos. Trans. R. Soc. London A* **365**, 665 (2007).
- [84] S. C. C. Bailey, M. Hultmark, A. J. Smits, and M. P. Schultz, Azimuthal structure of turbulence in high Reynolds number pipe flow, *J. Fluid Mech.* **615**, 121 (2008).
- [85] L. H. O. Hellström, A. Sinha, and A. J. Smits, Visualizing the very-large-scale motions in turbulent pipe flow, *Phys. Fluids* **23**, 011703 (2011).
- [86] L. H. O. Hellström and A. J. Smits, The energetic motions in turbulent pipe flow, *Phys. Fluids* **26**, 125102 (2014).
- [87] L. H. O. Hellström, B. Ganapathisubramani, and A. J. Smits, The evolution of large-scale motions in turbulent pipe flow, *J. Fluid Mech.* **779**, 701 (2015).
- [88] L. H. O. Hellström, I. Marusic, and A. J. Smits, Self-similarity of the large-scale motions in turbulent pipe flow, *J. Fluid Mech.* **792**, R1 (2016).
- [89] L. H. O. Hellström and A. J. Smits, Structure identification in pipe flow using proper orthogonal decomposition, *Philos. Trans. R. Soc. London A* **375**, 20160086 (2017).
- [90] L. H. O. Hellström, T. Van Buren, J. Vaccaro, and A. J. Smits, Complete eddy self-similarity in turbulent pipe flow, [arXiv:1911.10539](https://arxiv.org/abs/1911.10539).
- [91] L. H. O. Hellström, B. Ganapathisubramani, and A. J. Smits, The evolution of large-scale motions in turbulent pipe flow – Corrigendum, *J. Fluid Mech.* **795**, 973 (2016).
- [92] D. J. C. Dennis and T. B. Nickels, Experimental measurement of large-scale three-dimensional structures in a turbulent boundary layer. Part 2. Long structures, *J. Fluid Mech.* **673**, 218 (2011).